INTERNATIONAL JOURNAL FOR NUMERICAL METHODS IN FLUIDS
Int. J. Numer. Meth. Fluids 2005; **49**:1213–1232
Published online 11 August 2005 in Wiley InterScience (www.interscience.wiley.com). DOI: 10.1002/fld.1021

Hybrid finite-volume finite-difference scheme for the solution of Boussinesq equations

K. S. Erduran[1,*,†], S. Ilic[1,‡] and V. Kutija[2]

[1]*Physics Building, Department of Geography, University of Lancaster, LA1 4YN, U.K.*
[2]*WRSRL, Cassie Building, Department of Civil Engineering, University of Newcastle upon Tyne, NE1 7RU, U.K.*

SUMMARY

A hybrid scheme composed of finite-volume and finite-difference methods is introduced for the solution of the Boussinesq equations. While the finite-volume method with a Riemann solver is applied to the conservative part of the equations, the higher-order Boussinesq terms are discretized using the finite-difference scheme. Fourth-order accuracy in space for the finite-volume solution is achieved using the MUSCL-TVD scheme. Within this, four limiters have been tested, of which van-Leer limiter is found to be the most suitable. The Adams–Basforth third-order predictor and Adams–Moulton fourth-order corrector methods are used to obtain fourth-order accuracy in time. A recently introduced surface gradient technique is employed for the treatment of the bottom slope. A new model 'HYWAVE', based on this hybrid solution, has been applied to a number of wave propagation examples, most of which are taken from previous studies. Examples include sinusoidal waves and bi-chromatic wave propagation in deep water, sinusoidal wave propagation in shallow water and sinusoidal wave propagation from deep to shallow water demonstrating the linear shoaling properties of the model. Finally, sinusoidal wave propagation over a bar is simulated. The results are in good agreement with the theoretical expectations and published experimental results. Copyright © 2005 John Wiley & Sons, Ltd.

KEY WORDS: hybrid scheme; finite-volume scheme; Boussinesq model; fourth-order accuracy; deep-water wave propagation; deep to shallow water wave propagation

1. INTRODUCTION

Over the last few decades, several numerical models have been developed to predict wave propagation from relatively deep to shallow water. The most advanced numerical models are

*Correspondence to: K. S. Erduran, Hydraulic Division, Civil Engineering Department, University of Nigde, 51100 Nigde, Turkey.
†E-mail: kserduran@nigde.edu.tr, kerduran@hotmail.com
‡E-mail: s.ilic@lancaster.ac.uk

Contract/grant sponsor: U.K. Engineering and Physical Sciences Research Council (EPSRC); contract/grant number: GR/R79227/01

Received 21 August 2003
Revised 11 October 2004
Accepted 26 May 2005

thus far based on various forms of the Boussinesq equations [1–3]. Boussinesq [4] originally developed these equations in 1872, by incorporating low-order dispersive effects into the non-linear shallow water equations for waves propagating over a horizontal bottom. Peregrine [5] re-derived a system of Boussinesq equations to describe the non-linear transformation of irregular short waves in water of varying depth in terms of depth-averaged velocities. Since these equations were limited to shallow water, further efforts have been made to extend the applicability of the equations to deep water. Madsen *et al.* [6] and Madsen and Sorensen [1] added an extra dispersive term to a modified form of Peregrine's equations; Nwogu [2] derived new equations by choosing the velocity at an arbitrary depth as one of the variables; while Beji and Nadaoka [3] applied algebraic manipulation to Peregrine's original equations. These modified equations describe weak non-linear and weak dispersive water waves in variable depths of water. It has been shown that they provide a reasonably good description of wave propagation in coastal regions [7].

Significant efforts have been made in the past to solve these equations numerically, and different solution approaches have been introduced. Most of the numerical solutions are based on the finite-difference method [1–3, 8, 9], although there are examples of finite-element solutions [10–13]. The earliest application of the finite-difference method [8, 14] showed that the truncation errors of low-order approximations significantly affect the accuracy of the solution. This is because the truncation errors of the finite-difference approximations are of the same form as the dispersive terms in the Boussinesq equations. Hence, these errors lead to the prediction of non-physical dispersion or 'numerical diffusion'. In order to eliminate this effect and obtain accurate solutions, a careful treatment of truncation errors is necessary. For example, Abbott *et al.* [8] substitute the truncation error terms back into their original second-order scheme. Alternatively, Wei *et al.* [14] used higher-order techniques for spatial discretization and time integration, avoiding truncation error terms of the same order as the dispersive terms.

On the other hand, the finite-element methods can be applied more easily to complex coastal regions than the finite-difference methods. However, it is not easy to apply these methods directly to the extended form of equations [1–3]. Recently, Walkley and Berzins [10] rewrote Nwogu's [2] equations and applied the finite element method successfully. They demonstrated that highly accurate solutions of wave propagation could be obtained by using this method. For example, the truncation errors, for the applied linear second-order finite-element method for spatial discretization on a regular uniform mesh, were of the same form as those obtained by Wei *et al.* [14]. While their finite-element solution is applicable to a non-uniform mesh, the solution can produce non-physical dispersion, the degree of which depends on the selected mesh size [10]. Hence, the variation of mesh size needs to be suitably controlled. In summary, both finite-difference and finite-element methods give comparable solutions.

In the last decade, the finite-volume method has been used widely for the solution of the non-linear shallow water equations [15–18] leading to much improved predictions of flows in shallow water. The method is particularly successful for shock waves and the complex domain. Unfortunately, the Boussinesq equations do not lend themselves easily to the finite-volume method. Recently, a hybrid solution, combining the finite-volume and difference methods, has been introduced for the Boussinesq-like equations [19]. This new hybrid solution has been compared with the finite-difference solution by applying both methods for the simulation of secondary free-surface undulations (Favre waves). It has been concluded that the hybrid solution produces more accurate results than the finite-difference solution for wave profiles that are initially steep [19]. This provides the opportunity to develop an integrated model

based on a hybrid solution of governing equations to simulate the wave propagation from deep to swash zone.

In this study, we have developed a new hybrid solution to a one-dimensional (1D) Boussinesq equations, in order to simulate the wave propagation from deep to shallow water. Although Nwogu's [2] and Beji and Nadaoka's [3] equations appear to have better linearized dispersion characteristics, Madsen and Sørensen's [1] equations were here chosen as the most suitable for the application of the finite-volume technique. The application of the hybrid scheme required the governing equations to be recast to obtain a conservative part that suits the finite-volume discretization. The conservative part includes the continuity equation and part of the momentum equations (acceleration term and convective momentum terms). The remaining terms in the momentum equations, namely the higher order dispersive non-linear Boussinesq terms, the friction and the bottom slope terms, are considered as the source and the sink terms. The conservative part is discretized using the finite-volume method with the Roe scheme [20] whereas the source and sink terms are discretized using the finite-difference method.

Since the application of the finite-difference method is straightforward, the aim of this paper is to present the details of the finite-volume solution. In analogy to Wei *et al.* [14] where (neglecting the bottom slope) there is a fourth-order finite-difference discretization of the first-order derivative terms, the hybrid method applies fourth-order discretization in space and time. High-order discretizations are essential to provide accurate solutions. For the first-order spatial derivative terms in the conservative part, the so-called fourth-order accurate compact MUSCL (monotone upstream-centred schemes for conservation laws)-TVD (total variation diminishing) scheme [21] is used. The bottom slope requires a special treatment as in the finite-volume solution of the non-linear shallow water equations [22–25]. This work uses the surface gradient method, introduced by Zhou *et al.* [25] for the second-order solution of the non-linear shallow water equations. They showed that this method is accurate for providing flux balances in the existence of variable topography when higher order solution techniques are used. A fourth-order accurate solution in time is provided using the third-order predictor scheme of Adams–Basforth followed by the fourth-order corrector scheme of Adams–Moulton [14]. The continuity equation is solved explicitly, whereas the momentum equation is solved implicitly, using a double-sweep algorithm [26]. The governing equations and numerical solutions are given in more detail in Section 2.

The newly developed model has been tested by applying it to a number of examples of wave propagation, largely taken from the literature. These examples are: sinusoidal wave propagation in deep and shallow waters over a flat bottom; bi-chromatic wave propagation over a flat bottom; sinusoidal wave propagation from deep to shallow water over a slope of $\frac{1}{50}$; and a periodic wave propagating over a bar. The results obtained are compared with published and theoretical results and are presented in Section 3. Discussion of the performance of the hybrid solution is given in Section 4. Finally, conclusions and further recommendations are given in Section 5.

2. METHODOLOGY

In this section, we give details of the governing Boussinesq equations and describe their numerical solution. Madsen *et al.* [6] and Madsen and Sorensen [1] re-derived the Boussinesq

equations originally introduced by Peregrine [4] using depth-integrated velocities (i.e. fluxes) instead of depth-averaged velocity components and extended their dispersive characteristics. This system of extended equations is applicable for irregular wave propagation on a slowly varying bathymetry from deep to shallow water. For these purposes, the deep-water limit corresponds to $d/L_0 = 0.5$, where d is the still water depth and L_0 is the deep-water wavelength.

The following are the Madsen and Sørensen [1] Boussinesq-type equations:

$$\frac{\partial \eta}{\partial t} + \frac{\partial P}{\partial x} = 0 \tag{1}$$

$$\frac{\partial P}{\partial t} + \frac{\partial}{\partial x}\left(\frac{P^2}{h}\right) + gh\frac{\partial \eta}{\partial x} + \psi_x + \frac{\tau_x}{\rho} = 0 \tag{2}$$

where η is surface elevation measured from the still water depth (d), $P(P = hu)$ is the volume flux and u is the depth-averaged velocity in the x direction, h is the water depth and τ_x is the bottom shear stress in the x direction. The symbol ψ_x denotes the higher order Boussinesq terms, explicitly given as

$$\psi_x \equiv -\left(B + \frac{1}{3}\right) d^2 \left(\frac{\partial^3 P}{\partial x^2 \partial t}\right) - Bgd^3 \left(\frac{\partial^3 \eta}{\partial x^3}\right) - d\frac{\partial d}{\partial x}\left(\frac{1}{3}\frac{\partial^2 P}{\partial x \partial t} + 2Bgd\frac{\partial^2 \eta}{\partial x^2}\right) \tag{3}$$

where B is a coefficient, set equal to $\frac{1}{15}$ as suggested by Madsen and Sørensen [1]. The terms used in Equations (1) and (2) are graphically presented in Figure 1.

The Boussinesq equations given in Equations (1) and (2) are well suited to our hybrid solution method in which a finite-volume scheme is applied to conservative part in combination with a finite-difference scheme applied to the remaining terms.

In order to obtain conservative forms of Equations (1) and (2), it is assumed that the bottom elevation (topography) is not changing with time or that changes are small in comparison with surface elevation changes:

$$\frac{\partial \eta}{\partial t} = \frac{\partial h}{\partial t} \tag{4}$$

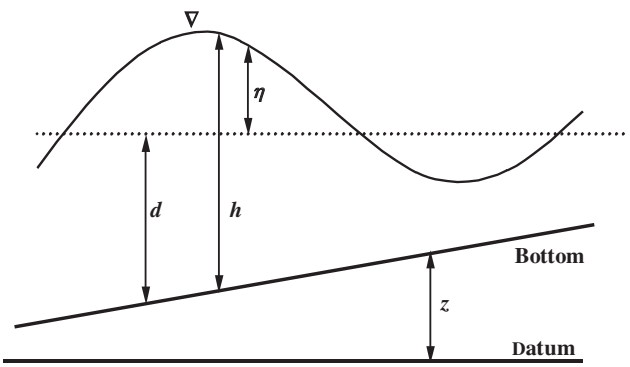

Figure 1. Symbols used in 1D Boussinesq equations.

because

$$\frac{\partial \eta}{\partial t} = \frac{\partial (h-d)}{\partial t} = \frac{\partial h}{\partial t} - \frac{\partial d}{\partial t} \quad \text{as} \quad \frac{\partial d}{\partial t} = 0$$

and

$$gh\frac{\partial \eta}{\partial x} = gh\frac{\partial}{\partial x}(h-d) = \frac{\partial}{\partial x}\left(\frac{1}{2}gh^2\right) - gh\frac{\partial d}{\partial x} \tag{5}$$

Also, the derivative of the still water depth, d, with respect to x represents the bottom variation in the x direction and can be rewritten as

$$gh\frac{\partial d}{\partial x} = -gh\frac{\partial z}{\partial x} \tag{6}$$

where z is the bottom elevation measured from the datum (Figure 1). The left-hand side of Equation (6) is known as the bottom slope term.

By introducing Equations (4)–(6) into Equations (1) and (2), the continuity and momentum equations read:

$$\frac{\partial h}{\partial t} + \frac{\partial hu}{\partial x} = 0 \tag{7}$$

$$\frac{\partial hu}{\partial t} + \frac{\partial}{\partial x}\left(hu^2 + \frac{1}{2}gh^2\right) - gh\frac{\partial z}{\partial x} + \psi_x + \frac{\tau_x}{\rho} = 0 \tag{8}$$

Hence, in compact-conservative form, Equations (7) and (8) take the vector form

$$\frac{\partial \mathbf{q}}{\partial t} + \frac{\partial \mathbf{f}(\mathbf{q})}{\partial x} = \mathbf{b}(\mathbf{q}) \tag{9}$$

where $\mathbf{q} = (h, hu)^{\mathrm{T}}$ is the so-called conservative physical vector, $\mathbf{f}(\mathbf{q}) = (hu, hu^2 + \frac{1}{2}gh^2)^{\mathrm{T}}$ is the flux vector. The vector $\mathbf{b}(\mathbf{q}) = (0, gh(So_x - Sf_x) - \psi_x)^{\mathrm{T}}$ is used to denote the source/sink terms, where $So_x = gh(\partial z/\partial x)$ is the bottom slope and Sf_x is the friction term that can be given by Manning's Formula as

$$Sf_x = \frac{n^2 u^2}{h^{4/3}} \tag{10}$$

Hence a hybrid solution can be applied to the re-caste Equations (7) and (8). Numerical solutions are given in following sections.

2.1. Solution

First Equations (7) and (8) are rewritten following Wei *et al.* [14], as

$$h_t = E \tag{11}$$

$$U_t = F \tag{12}$$

where

$$U_t = [hu]_t - (B + \tfrac{1}{3})d^2 P_{xxt} - d d_x \tfrac{1}{3} P_{xt}$$

$$E = -[hu]_x$$

$$F = -[hu^2 + \tfrac{1}{2}gh^2]_x + ghz_x - ghSf_x + Bgd^3\eta_{xxx} + 2Bd^2 d_x \eta_{xx}$$

and the subscript t denotes time derivative while subscript x denotes space derivative.

2.2. Discretization in space

Applying the finite-volume method, the spatial discretization of the continuity equation, E, results in

$$E = -\frac{1}{A}\sum_{w=1}^{m} \mathbf{T}^{-1}(\theta^w)\mathbf{f}_1^w(\tilde{\mathbf{q}}^w)L^w \tag{13}$$

where A is the area of the cell, m is the number of sides of the cell, w is an index that represents the side, $\mathbf{T}(\theta^w)$ is the transformation matrix which can be obtained by rotating the co-ordinate axes, $\mathbf{T}^{-1}(\theta^w)$ is the inverse transformation matrix, L^w is the length of the wth cell side, θ^w is the angle between the outward normal vector $\mathbf{n}$ and the x-axis, $\tilde{\mathbf{q}}^w$ is the transformed conservative physical (variable) vector obtained by multiplying $\mathbf{q}$ by the transformation matrix and $\mathbf{f}_1^w(\tilde{\mathbf{q}}^w)$ refers to a numerical mass flux, related to the first component, h. More detailed information on how the transformation matrix $\mathbf{T}(\theta^w)$ and its inverse matrix $\mathbf{T}^{-1}(\theta^w)$ were constructed can be found in Reference [27]. As the solution given here is for the 1D Boussinesq equations, θ^w can take only two values; 0° and 180°. Also, there are only two active interfaces for each cell in the x directions.

The spatial discretized form of F by combining finite-volume and finite-difference methods can be given as

$$\begin{aligned} F = &-\frac{1}{A}\sum_{w=1}^{m} \mathbf{T}^{-1}(\theta^w)\mathbf{f}_2^w(\tilde{\mathbf{q}}^w)L^w - gh_i\left(\frac{z_{i+1/2} - z_{i-1/2}}{\Delta x}\right) - gh_i Sf_x \\ &+ \frac{Bg(d_i)^3}{2\Delta x^3}[\eta_{i+2} - 2\eta_{i+1} + 2\eta_{i-1} - \eta_{i-2}] \\ &+ \frac{Bg(d_i)^2}{6\Delta x^3}(-d_{i+2} + 8d_{i+1} - 8d_{i-1} + d_{i-2})[\eta_{i+1} - 2\eta_i + \eta_{i-1}] \end{aligned} \tag{14}$$

Here, $\mathbf{f}_2^w(\tilde{\mathbf{q}}^w)$ corresponds to the numerical momentum flux. The index i refers to the finite-volume cell as well as to the finite-difference grid point at the centre of ith finite-volume cell.

The finite-difference approximation of the sources/sinks is given in Equation (14) while the numerical fluxes in Equations (13) and (14) are evaluated solving Riemann problems at the cell interfaces. In this study the Roe scheme [20] is used, although, any Riemann solvers such as HLL, HLLC and Osher [28] can be used instead. More detailed information about

the evaluation of numerical fluxes by solving Riemann problems can be found in Reference [27].

The finite-volume discretizations given in Equations (13) and (14) are suitable for both structured and unstructured cells. However, due to the inclusion of the finite-difference discretization, the solution given in here is restricted to use on rectangular grids only. Details of the 1D finite-volume part (i.e. integration and discretization in finite volume) of the hybrid solution can be found elsewhere [29, 30]. Here, we concentrate on higher order solutions only.

Higher order solutions by the finite-volume method can be achieved by construction of data on the cell interfaces prior to computation of numerical fluxes. In this work, the cell interface values are constructed using the fourth-order compact MUSCL-TVD scheme given by Yamamoto *et al.* [21]. These cell interface values are then used for the solution of Riemann problems. Due to the use of the surface gradient method, data construction for water depth, h, is completed using the surface level (H) gradient as explained below.

First, the surface level is defined at the centre of a cell as $H = h + z$ where z is a bed elevation at the centre of a cell (from an arbitrary level) and it is assumed that [25]

$$z_i = \frac{z_{i+1/2} + z_{i-1/2}}{2}$$

where $z_{i+1/2}$ and $z_{i-1/2}$ are the bed elevations at cell interfaces; $i + \frac{1}{2}$ and $i - \frac{1}{2}$, respectively, and they are given as an input to the model.

Following Yamamoto *et al.* [21], the fourth-order construction is done as follows:

$$H^{\mathrm{L}}_{i+1/2} = H_i + [\varphi(r_1)\Delta^* H_{i-1/2} + \varphi(1/r_1)2\Delta^* H_{i+1/2}]/6 \tag{15}$$

$$H^{\mathrm{R}}_{i+1/2} = H_{i+1} - [\varphi(r_2)2\Delta^* H_{i+1/2} + \varphi(1/r_2)\Delta^* H_{i+3/2}]/6 \tag{16}$$

where $H^{\mathrm{L}}_{i+1/2}$ is the surface level at the left-hand side of the interface $i + \frac{1}{2}$ and $H^{\mathrm{R}}_{i+1/2}$ is the surface level at the right-hand side of the interface $i + \frac{1}{2}$.

The inside of the cell under consideration always corresponds to the left-hand side of the interface, and the neighbouring cell to the right-hand side.

The values of $\Delta^* H$ are calculated in following way:

$$\Delta^* H_{i+1/2} = \Delta H_{i+1/2} - \Delta^3 \bar{H}_{i+1/2}/6, \quad \Delta H_{i+1/2} = H_{i+1} - H_i$$

$$\Delta^3 \bar{H}_{i+1/2} = \Delta \bar{H}_{i+3/2} - 2\Delta \bar{H}_{i+1/2} + \Delta \bar{H}_{i-1/2}$$

$$\Delta \bar{H}_{i-1/2} = m(\Delta H_{i-1/2}, \Delta H_{i+1/2}, \Delta H_{i+3/2})$$

$$\Delta \bar{H}_{i+1/2} = m(\Delta H_{i+1/2}, \Delta H_{i+3/2}, \Delta H_{i-1/2})$$

$$\Delta \bar{H}_{i+3/2} = m(\Delta H_{i+3/2}, \Delta H_{i-1/2}, \Delta H_{i+1/2})$$

m denotes the Minmod limiter and is given as

$$m(j,k,l) = (S)\max[0, \min(|j|, b_2(S)k, b_2(S)l)]$$

where $S = \mathrm{sign}(j)$ and $b_2 = 2$.

By eliminating the term $\Delta^3 \bar{H}_{i+1/2}$, the ordinary third-order MUSCL scheme can be retrieved. The function $\varphi(r_1)$ for the use of van-Leer limiter is defined as

$$\varphi(r_1) = \frac{r_1 + |r_1|}{1 + r_1}, \quad \text{and similarly for } r_2$$

where

$$r_1 = \frac{\Delta^* H_{i+1/2}}{\Delta^* H_{i-1/2}}, \quad r_2 = \frac{\Delta^* H_{i+3/2}}{\Delta^* H_{i+1/2}}$$

Generally, flux or slope limiters [31] are used in order to avoid the occurrence of possible over- or under-shoots due to the higher order MUSCL discretization. The well-known slope limiters are: van-Leer, Minmod, Superbee and van-Albada [31]. The original method introduced by Yamamoto *et al.* [21] uses the Minmod limiter in both third- and fourth-order compact terms. However, numerical tests within this study show that the use of the van-Leer limiter for the third-order part gives more accurate results. Consequently the van-Leer limiter is used in the proposed model for the third-order part and the Minmod for the fourth-order part. The use of slope limiters will be further discussed later in Section 4.

Finally, the construction of cell interface values for h is completed by

$$h^{\mathrm{L}}_{i+1/2} = H^{\mathrm{L}}_{i+1/2} - z_{i+1/2} \quad \text{and} \quad h^{\mathrm{R}}_{i+1/2} = H^{\mathrm{R}}_{i+1/2} - z_{i+1/2} \tag{17}$$

It may be worth mentioning here that the central second-order approximation is used for the discretization of the bottom slope as shown in Equation (14), and it gives accurate flux balances. The above procedure is applied to data construction at the interface $(i - \frac{1}{2})$. For the construction of the volume fluxes P, H is replaced by P in Equations (15) and (16) and Equation (17) is not used.

2.3. Time integration

Time integration is achieved in two stages, namely the third-order Adams–Basforth predictor stage and the fourth-order Adams–Moulton corrector stage. These stages are detailed below:

1. *Predictor stage* (*Adams–Basforth method*)

$$h^{n+1} = h^n + \frac{\Delta t}{12}[23E^n - 16E^{n-1} + 5E^{n-2}] \tag{18}$$

$$U^{n+1} = U^n + \frac{\Delta t}{12}[23F^n - 16F^{n-1} + 5F^{n-2}] \tag{19}$$

2. *Corrector stage* (*Adams–Moulton method*)

$$h^{n+1} = h^n + \frac{\Delta t}{24}[9E^{n+1} + 19E^n - 5E^{n-1} + E^{n-2}] \tag{20}$$

$$U^{n+1} = U^n + \frac{\Delta t}{24}[9F^{n+1} + 19F^n - 5F^{n-1} + F^{n-2}] \tag{21}$$

U^n and U^{n+1} are explicitly given in Equations (22) and (23), respectively.

$$U^n = P_i^n + K1[-P_{i+1}^n + 2P_i^n - P_{i-1}^n] + \frac{K2}{72}[-P_{i+1}^n + P_{i-1}^n] \tag{22}$$

where

$$K1 = \left(B + \frac{1}{3}\right)\left(\frac{(d_i^n)^2}{\Delta x^2}\right) \tag{23}$$

and

$$K2 = \frac{d_i^n}{\Delta x^2}(-d_{i+2}^n + 8d_{i+1}^n - 8d_{i-1}^n + d_{i-2}^n)$$

$$U^{n+1} = \left[-K1 + \frac{K2}{72}\right] P_{i-1}^{n+1} + [1 + 2K1]P_i^{n+1} - \left[K1 + \frac{K2}{72}\right] P_{i+1}^{n+1}$$

As can be clearly seen, the water depth in the next time level can be explicitly evaluated from Equations (18) and (20). However, Equations (19) and (21) require implicit solution. For that purpose, these equations are rearranged as follows:

$$A1 = \left[-K1 + \frac{K2}{72}\right], \quad B1 = [1 + 2K1], \quad C1 = -\left[K1 + \frac{K2}{72}\right]$$

and

$$D1 = P_i^n + K1[-P_{i+1}^n + 2P_i^n - P_{i-1}^n] + \frac{K2}{72}[-P_{i+1}^n + P_{i-1}^n] + \frac{\Delta t}{12}[23F^n - 16F^{n-1} - 5F^{n-2}]$$

$$D2 = P_i^n + K1[-P_{i+1}^n + 2P_i^n - P_{i-1}^n] + \frac{K2}{72}[-P_{i+1}^n + P_{i-1}^n] + \frac{\Delta t}{24}[9F^{n+1} + 19F^n - 5F^{n-1} + F^{n-2}]$$

$$A1P_{i-1}^{n+1} + B1P_i^{n+1} + C1P_{i+1}^{n+1} = D1 \tag{24}$$

$$A1P_{i-1}^{n+1} + B1P_i^{n+1} + C1P_{i+1}^{n+1} = D2 \tag{25}$$

where Equations (24) and (25) are rearranged forms of Equations (19) and (21), respectively.

In the predictor stage, a system of simultaneous linear equations, produced by the application of Equation (24) at every grid point, is solved. In the corrector stage, the same procedure is repeated for Equation (25). These systems of linear equations are solved by the double-sweep algorithm [26]. As suggested by Wei *et al.* [14], the corrector stage is repeated if the error between two successive results measured by Δf given in Equation (26), exceeds 0.001. The values calculated in the corrector step are considered to be the final next time step $(n+1)$ values only when $\Delta f < 0.001$.

$$\Delta f = \frac{\sum_i |f_i^{n+1} - f_i^{(n+1)*}|}{\sum_i |f_{i^{n+1}}|} \tag{26}$$

where f represents any of the variables (h and P) and * denotes the previous iteration.

The overall solution can be summarized as follows:

1. Data construction is completed for each cell interfaces and numerical fluxes are evaluated solving Riemann problems at these cell interfaces.
2. Using Equations (13) and (14), the values of E and F are calculated.
3. The explicit Equation (18) is used to compute the predictor values of h.
4. The implicit Equation (19), rearranged and written in the form of Equation (24), is solved by double-sweep algorithm. The solution then gives the predicted values of $(P = hu)$. This completes the predictor stage.
5. Steps 1 and 2 are repeated. However, the next time step values of E and F in Equations (20) and (21) are computed using the predictor values.
6. The explicit Equation (20) is used to compute the corrected values of h, which are considered as the final time step values if $\Delta f < 0.001$.
7. The implicit Equation (21) is rearranged and written in the form of Equation (25), and again solved by the double-sweep algorithm. The solution then gives the corrected values of P (hu). The same condition, $\Delta f < 0.001$, should also be provided. Once the condition is achieved the final values of P are considered to be the next time step values of P (i.e. P^{n+1}).

3. TESTS AND RESULTS

Based on the methodology introduced in Section 2, a new numerical model called HYWAVE (Hybrid WAVE model) has been developed. The use of the object oriented language DELPHI 5 eased the development of graphical user interfaces for data input and output of intermediate and final results. A series of numerical tests have been performed in order to validate the model performance. Here, the model applications to five examples taken from previous studies [1, 6, 7, 10, 32] are presented. All of the following test cases are frictionless.

3.1. Test A: sinusoidal wave propagation in deep waters

The first test of a sinusoidal wave propagating in a channel with a horizontal bottom taken from Reference [6]. The channel is 120 m long and the still water depth is 4.2 m. The period and amplitude of the sinusoidal wave are 2.5 s and 0.1 m, respectively. In this case the ratio of water depth and wavelength, $d/L_0 = 0.43$, is closed to the deep-water limit, $d/L_0 = 0.5$. At the seaward boundary, a sinusoidal wave is generated and at the shoreward boundary a sponge layer [14, 33] is introduced to absorb the incoming wave. The time step chosen is 0.02 s. A satisfactory result was obtained with a spatial grid size of 0.1875 m, resulting in 650 cells being used. Throughout this study, all finite-volume cells have a unit length in the direction perpendicular to x-axis. For example in this test each finite-volume cell has a 0.1875×1 m size. The choice of grid size will be explained later in Section 4.

The simulated wave propagation is shown in Figure 2. The incoming wave is well developed and the effectiveness of the sponge layer can be clearly seen on the shoreward boundary (right end of the channel in Figure 2). The simulated wave amplitude is 0.1m and wavelength 9.97m. The wavelength was compared with the theoretical expectation from linear wave theory given

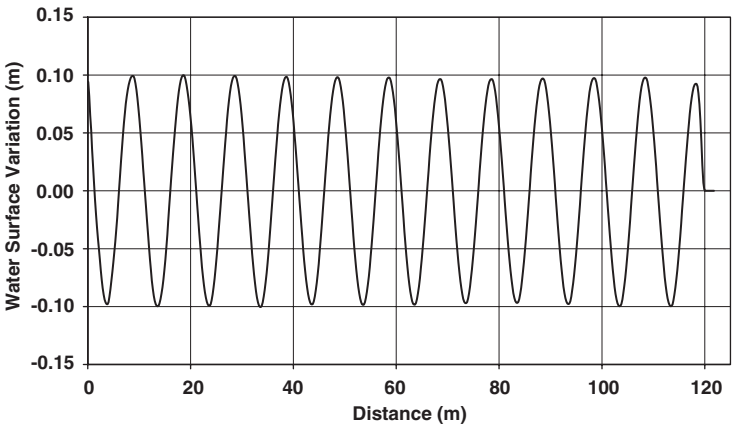

Figure 2. Surface elevation profile—sinusoidal wave propagation in deep water ($d/L_0 = 0.43$).

in Equation (27):

$$L = \left(\frac{gT^2}{2\pi}\right) \tanh\left(\frac{2\pi d}{L}\right) \tag{27}$$

A difference between the model and theoretical wavelengths was found to be 0.29 m, meaning that the model produces 3% celerity error. Although the magnitude of the error is the same as that reported by Madsen *et al.* [6], their error is opposite in sign (−3%). The fact that both models produced celerity errors could be arising from the dispersion characteristics of the Boussinesq equations. The difference in celerity errors between two models is most likely caused by the different numerical techniques used.

The second sinusoidal test in deep water is taken from Reference [10]. The test is set up in a 15 m long channel of constant depth of 0.56 m. The incoming wave that propagates into an initially undisturbed domain has a sinusoidal shape, a wave amplitude = 0.025 m and wave period = 0.85 s. Hence, the ratio d/L_0 is almost equal to 0.5, which is at the limit of applicability for the Boussinesq equations. At the seaward boundary, a sinusoidal wave is generated and at the shoreward boundary a sponge layer is used. For the model simulation, a time step of 0.01 s and grid size of 0.03 m, hence 500 cells are used.

Figure 3 shows the water surface elevation at $t = 40$ s. It can be seen that the incoming wave is well developed and that steady solution has been achieved. The modelled wavelength is 1.24 m whereas the wavelength according to the linear wave theory is 1.17 m. This indicates a celerity error of 4%, which is similar to the error in previous test. The result agrees well with that reported by Walkley and Berzins [10] despite the different form of Boussinesq equations and numerical solutions used.

For the final sinusoidal wave propagation test, the first sinusoidal example given in Reference [6] is repeated. Channel and flow properties are kept the same but the still water depth is increased to 5 m, resulting in $d/L_0 \approx 0.51$; hence the conditions are pushed outside the limits of extended Boussinesq equations. The theoretically expected wavelength in this case is 9.73 m. The simulated wave profile is given in Figure 4. Again, a steady solution with

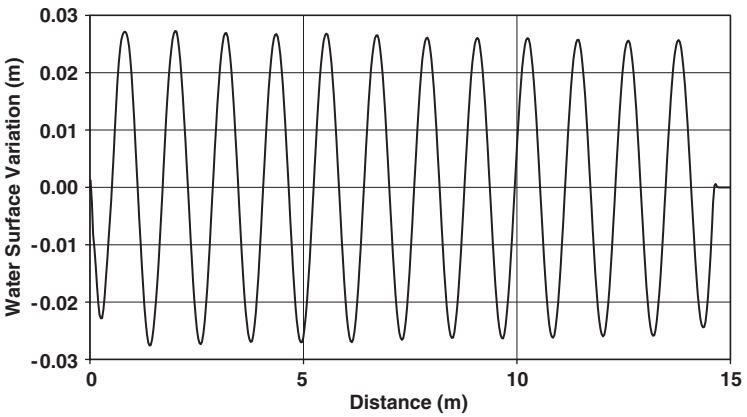

Figure 3. Surface elevation profile—sinusoidal wave propagation in deep water ($d/L_0 \approx 0.5$).

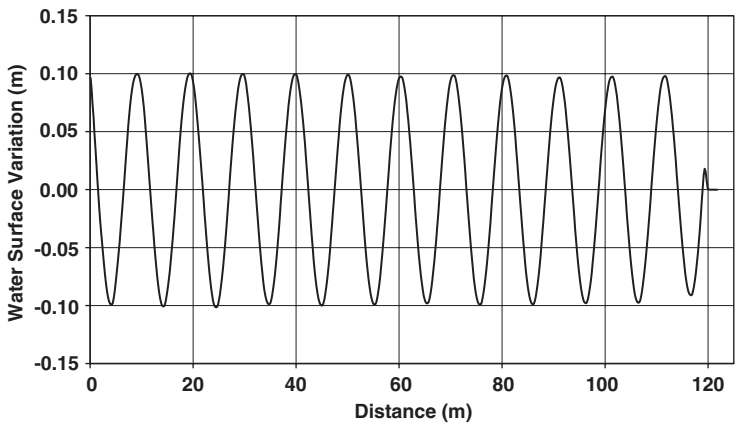

Figure 4. Surface elevation profile—sinusoidal wave propagation in deep water ($d/L_0 \approx 0.51$).

constant amplitude has been obtained. When looking at the model prediction, the wavelength is found to be 10.22 m thus the celerity error is estimated as 5%. This suggests that the error increases with increasing d/L_0.

These examples illustrated that the newly developed model can accurately predict the propagation up to the deep-water limits and that the results are comparable with results obtained with previously developed models.

The next test shows that the fourth-order solution in the new hybrid model is also applicable to the simulation of long wave motions. The Boussinesq equation is reduced to non-linear shallow water equations by neglecting the Boussinesq term (ψ_x) for this application. Then, the reduced model is applied to the sinusoidal wave propagation problem introduced by Hu *et al.* [32]. The channel is 1000 m long with flat bottom and still water depth of 10 m.

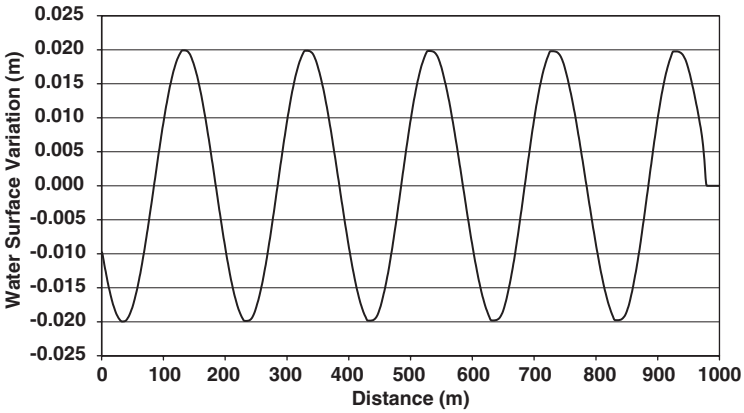

Figure 5. Surface elevation profile—sinusoidal wave propagation in shallow water.

A sinusoidal wave with a height of 0.04 m and a period of 20.193 s is generated at the seaward boundary. The ratio $d/L_0 \approx 0.016$ is close to the limit of shallow water conditions. At the shoreward boundary a sponge layer is used so that incoming wave passes through without reflection. This differs from original example [32] in which wave reflection is studied and the shoreward boundary is fully reflected off a closed boundary. The channel is divided into 1000 grids and time step of 0.02 s is used.

As can be seen in Figure 5, the model produces steady wave solution with a wavelength of 200 m, which agrees exactly with the reported wavelength [32] of 200 m. This last example shows that it is easy to 'switch' from the Boussinesq to non-linear-shallow water (NSW) model while keeping the finite-volume solution for NSW.

3.2. Test B: bi-chromatic wave propagation in deep water

Madsen *et al.* [6] simulated a bi-chromatic wave train in deep water. The same channel and still water depth given in the first sinusoidal test case are used. The wave consists of a combination of two waves; first one with a period of 2.5 s ($d/L_0 = 0.43$) and second one with a period of 3 s ($d/L_0 = 0.3$). Both waves have the same amplitude of 0.05 m. Taking into account previously observed errors for different d/L_0, it is encouraging to see that the model can produce a bi-chromatic wave train. The result at 12 m down from the seaward boundary is illustrated in Figure 6. The result is almost identical to that produced by Madsen *et al.* [6].

3.3. Test C: sinusoidal wave from deep to shallow water (linear shoaling)

Madsen and Sørensen [1] set up an example in order to verify their model with respect to linear shoaling. A channel 700 m long with combined flat and sloping bottom is chosen. The first 10 m from the seaward boundary have a constant depth of 13 m. Between 10 and 650 m, a slope of $\frac{1}{50}$ is introduced. Finally, from 650 to 700 m the bottom is flat again with a still water depth of 0.2 m. At the seaward boundary, a 4 s sinusoidal wave is generated whereas a sponge layer is applied at the shoreward boundary. In the model simulation, a 0.2 m spatial grid and a time step of 0.01 s are used.

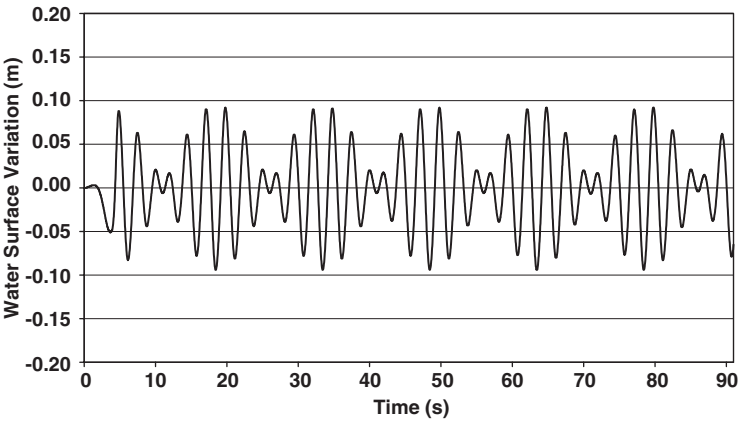

Figure 6. Surface elevation profile—bi-chromatic wave propagation in deep water.

In order to compute the linear shoaling of waves from deep to shallow water, Madsen and Sørensen [1] reduced the original momentum equation to Equation (28):

$$\frac{\partial P}{\partial t} + gd\frac{\partial \eta}{\partial x} + \psi_x = 0 \tag{28}$$

This modified momentum equation does not allow a solution in the form of a Riemann problem, as the slopes of the characteristics cannot be extracted. Therefore, further alterations have to be made in order to proceed with hybrid solution. Firstly, the modified momentum equation (28) is entirely discretized by the finite-difference method while the continuity equation remains to be discretized by the finite-volume method. In order to apply a Riemann solver, the slopes of characteristics are needed, which are calculated from the following equation:

$$\frac{\partial P}{\partial t} + gh\frac{\partial \eta}{\partial x} + \psi_x = 0 \tag{29}$$

This assumption yields the following slopes of the characteristics:

$$\lambda_1 = c, \quad \lambda_2 = -c \quad \text{or} \quad \lambda_1 = \sqrt{gh}, \quad \lambda_2 = -\sqrt{gh}$$

Despite this assumption not being entirely valid, no numerical problem has been detected. This is also demonstrated in Figure 7 where the results of the shoaling test agree with the theoretical one as well as the published one [1].

3.4. Test D: sinusoidal wave propagation over a bar

The bar-type geometry provides a rigorous test to distinguish the performance of models and it was used in the past to test the models based on Boussinesq-like approximations (e.g. References [7, 10]). The test is set up in a 25 m long channel with a flat bottom up to 6 m, a bar between 6 and 17 m and a flat bottom again between 17 m and the end of channel. The bar has an upward slope of 1:20 and steeper downward slope of 1:10. The channel depth is 0.4 m and the bar is 0.1 m below the surface at its highest point. A sinusoidal wave with

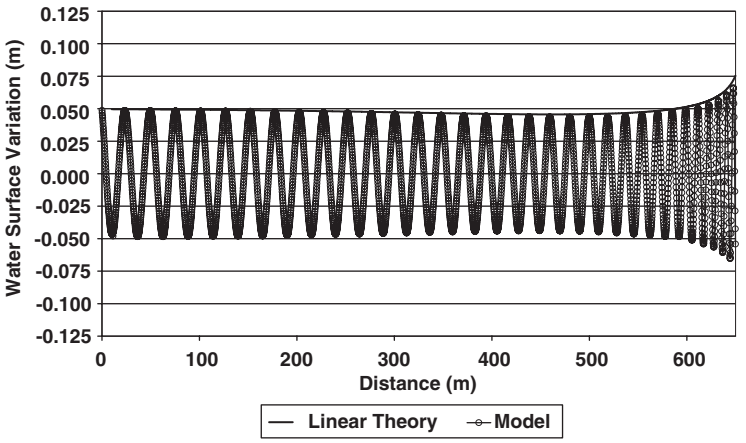

Figure 7. Free surface profile and maximum elevation envelope calculated by linear theory—sinusoidal wave propagation from deep water to shallow water ($\Delta x = 0.2$ m).

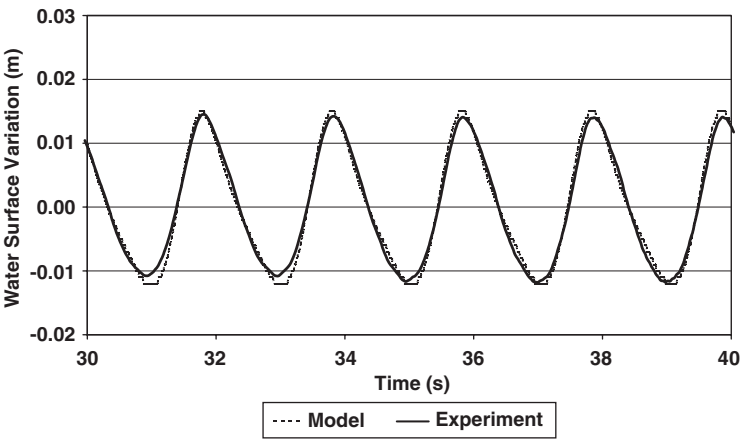

Figure 8. Time history of free surface profile at 10.5 m—sinusoidal wave propagation over a bar.

amplitude of 0.01 m and a period of 2.02 s is generated at the seaward boundary. A sponge layer is applied to the shoreward boundary as in the previous tests. The numerical simulation is performed with a time step of 0.007 s on a domain divided into 1000 cells, each of which has 0.025 m size.

The time histories of water surface profiles at points 10.5 m, 13.5 m, 15.7 m and 17.3 m are given in Figures 8–11, respectively. The results are in very good agreement with those measured [7] on the upward slope (at 10.5 m) and on the bar (at 13.5 m). However, discrepancies between the results and those measured occur on the downward slope and more obvious after the bar at 17.3 m. On the downward slope as the depth increases so does the

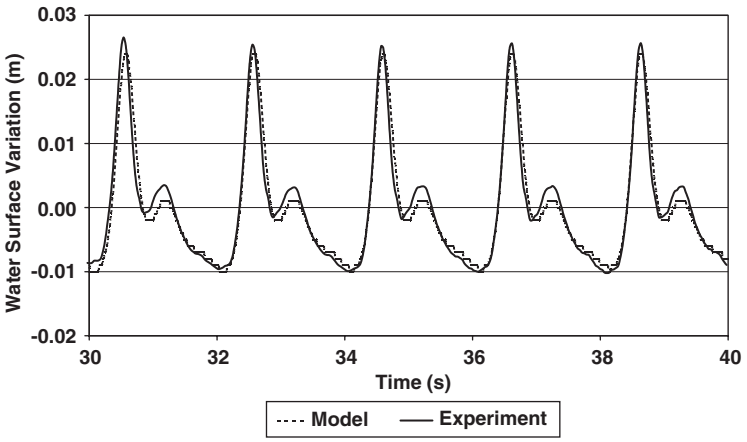

Figure 9. Time history of free surface profile at 13.5 m—sinusoidal wave propagation over a bar.

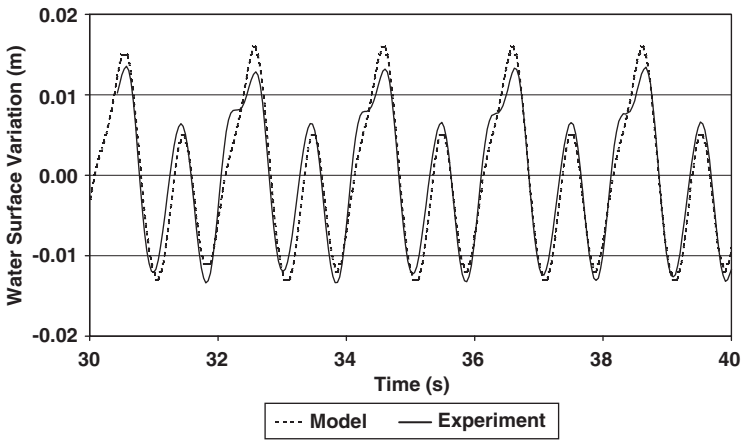

Figure 10. Time history of free surface profile at 15.7 m—sinusoidal wave propagation over a bar.

difference in celerity between the higher harmonic bound and free waves. Here, the difference between the predicted phase velocities and measured ones become more pronounced. This is in agreement with test performed by Dingemans [7] using Madsen and Sørensen model [1]. Also, the model results are quite similar to those obtained using an alternative set of equations and numerical techniques [10]. This indicates that the observed discrepancies are primarily due to the approximation of the dispersion relation in the governing equations [7].

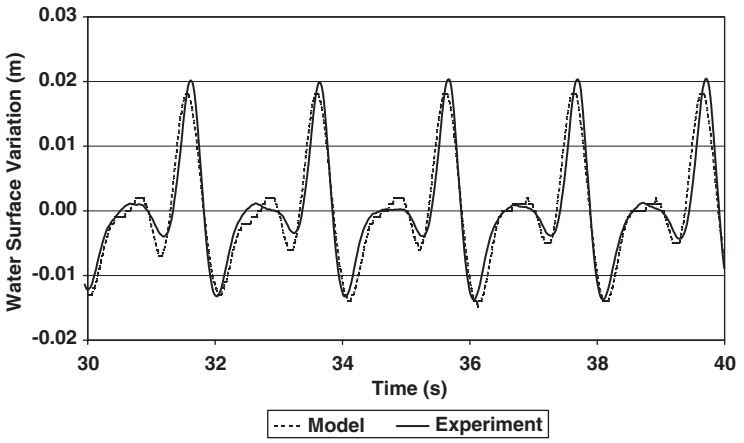

Figure 11. Time history of free surface profile at 17.3 m—sinusoidal wave propagation over a bar.

4. DISCUSSION

It has been demonstrated that the new hybrid finite-volume and finite-difference solution of extended Boussinesq equations [1] can produce accurate results. The hybrid method introduced here has an advantage over the entirely finite-difference solution in the discretization of the non-linear convective momentum term $\partial/\partial x(hu^2)$. Applying the finite-volume method, discretization is straightforward whereas it requires special attention if the finite-difference method is used [1]. This is in addition to the advantages, previously shown by Frazão and Zech [19], of using second-order MUSCL spatial discretization for the modelling of steep fronts.

However, in the examples shown, the grid size had to be chosen to be smaller than that reported in models based on the finite-difference solution [1]. Different numbers of grid points per wavelength were used in the different tests. The smallest number of grid points per wavelength, which was around 35, was used in Test C and that was sufficient to obtain accurate results. For example, Test C was repeated with a grid size of 0.5 m, and the result is shown in Figure 12. Although the linear shoaling is well captured by the model up to somewhere about 570 m, the discrepancies between the model and the linear theory increase towards the shoreward boundary. When the wave approaches the shallow region, the wavelength decreases and so does the number of grid points per wavelength. In other words, the condition explained earlier is satisfied until some point when the decreasing in wavelength violates the condition, and the amplitude of wave decreases as the solution becomes too diffusive. In addition, a smaller grid creates difficulties for the explicit computation of the continuity equation. The time step has to be chosen to be small enough that a stable solution can be achieved, and hence the simulation time gets longer.

The early investigations of this problem by the authors show that all the results presented here, except those for the shallow water application, depend heavily on the type of limiters used. The Superbee limiter is found to be unsuitable as it predicts too large wave heights. The Minmod limiter also fails to produce the correct wave heights and generally the incoming

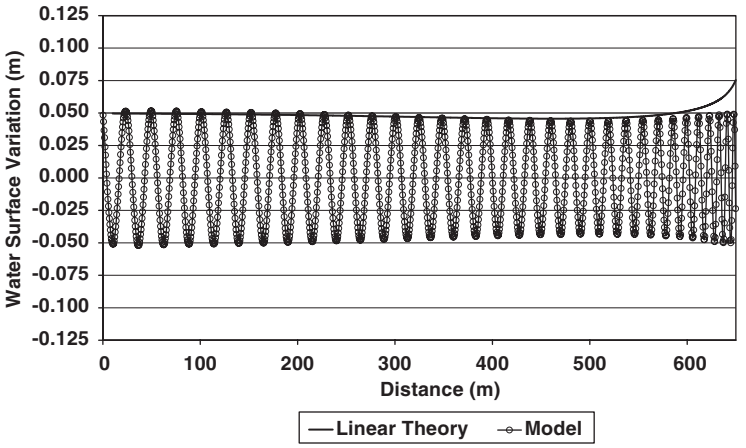

Figure 12. Free surface profile and maximum elevation envelope calculated by linear theory—sinusoidal wave propagation from deep water to shallow water ($\Delta x = 0.5$ m).

wave attenuates as it propagates shoreward. The van-Albada limiter behaves in a very similar manner to the Minmod limiter. The van-Leer limiter is found to have the least influence on propagating wave characteristics. Hence, the overall results were obtained using the van-Leer limiter in the third order part of the fourth-order compact MUSCL construction. Unfortunately, the application of the van-Leer limiter is not problem-free and it requires a certain number of grid points per wavelength in order to provide accurate results as explained above. Generally, it is known that reducing the grid size increases the accuracy of the solution. Here, however, different limiters can produce different results even though the same grid size is used.

The computational efficiency of the model could be improved if a suitable limiter is introduced. Generally, the Superbee limiter is the least diffusive and the Minmod limiter the most diffusive. This conclusion agrees with that reported by Bradford and Sanders [34]. The degree of diffusivity resulting from the use of the van-Leer limiter lies between the Superbee and Minmod limiters. A better solution can be achieved if a limiter with a degree of diffusivity between Superbee and van-Leer is provided. If such a limiter were used, the condition regarding the number of grid points per wavelength, would relax and larger grid and time step could be used.

5. CONCLUSION AND FURTHER STUDIES

The following conclusions can be drawn:

1. A new hybrid scheme, combining the finite-volume and difference approaches, is introduced for the solution of the Boussinesq equations in order to simulate wave propagation in deep water, from deep to shallow water and over a bar.
2. Fourth-order accuracy in space and time is used to avoid numerical diffusion. The fourth-order compact MUSCL scheme is applied for the finite-volume discretization of the

first-order derivative terms. Ordinary finite-difference discretization is applied to remaining terms. A surface gradient method is used to provide accurate flux balances at the cell interfaces in the vicinity of the bottom slope. The third-order Adams–Basforth predictor and the fourth-order Adams–Moulton corrector methods are employed to achieve fourth-order accuracy in time.

3. A numerical model has been developed and applied to several test cases. The results are in a good agreement with both the published experimental and theoretical results.
4. Four limiters (Superbee, Minmod, van-Albada and van-Leer) were tested and the van-Leer limiter was found to be the most suitable but at a cost that a number of grid points per wavelength should not be less than around 35.
5. The numerical solution has the advantage over a finite-difference solution alone that there is no need for special attention for the treatment of the non-linear convective term. This new numerical solution is compatible with solutions for nonlinear shallow water equations that are currently the most advanced and accurate numerical solutions for this type of equation. Hence, by neglecting the higher-order Boussinesq terms the solution can be used for the simulation of river flow and bore waves in both subcritical and supercritical forms crossing a step or wall [32]. However, the potential of this model lies in applications that require both Boussinesq and shallow water solutions.

Further studies will involve the full investigation of the slope limiters for the construction of data in higher order finite-volume solutions. The experiences suggest that the most suitable limiter would lie between the Superbee and the van-Leer with regard to the degree of diffusivity. Providing such a limiter would ease the restriction on the selection of a number of grid points per wavelength. Consequently, a larger grid size and so a time step would be used, resulting in a shorter simulation time. A 2D extension of the solution is under development.

ACKNOWLEDGEMENTS

This work was supported through funding by the U.K. Engineering and Physical Sciences Research Council (EPSRC) Grant Ref. GR/R79227/01. The authors would like to thank Dr M. W. Dingemans for providing the experimental results used in Test D.

REFERENCES

1. Madsen PA, Sørensen OR. A new form of the Boussinesq equations with improved linear dispersion characteristics. Part 2. A slowly-varying bathymetry. *Coastal Engineering* 1992; **18**:183–204.
2. Nwogu O. Alternative form of Boussinesq equations for nearshore wave propagation. *Journal of Waterway, Port, Coastal, and Ocean Engineering* 1993; **119**:618–638.
3. Beji S, Nadaoka K. A formal derivation and numerical modelling of the improved Boussinesq equations for varying depth. *Ocean Engineering* 1996; **23**:691–704.
4. Boussinesq J. Théorie des ondes et des ramous qui se propagent le long d'un canal rectangulaire horizontal. *Journal de Mathématique Pures et Appliquées, Deuxiéme Série* 1872; **17**:55–108.
5. Peregrine DH. Long waves on a beach. *Journal of Fluid Mechanics* 1967; **27**:815–827.
6. Madsen PA, Murray R, Sørensen OR. A new form of the Boussinesq equations with improved linear dispersion characteristics. *Coastal Engineering* 1991; **15**:371–388.
7. Dingemans M. *Water Wave Propagation Over Uneven Bottoms*. Advance Series in Ocean Engineering, vol. 13, Part 2. World Scientific: Singapore, 1997.
8. Abbott MB, McCowan AD, Warren IR. Accuracy of short-wave numerical models. *Journal of Hydraulic Engineering* 1984; **110**:1287–1301.
9. Karambas ThV, Koutitas C. A breaking wave propagation model based on the Boussinesq equations. *Coastal Engineering* 1992; **18**:1–19.

10. Walkley M, Berzins M. A finite element method for the one-dimensional extended Boussinesq equations. *International Journal for Numerical Methods in Fluids* 1999; **29**:143–157.
11. Walkley M, Berzins M. A finite element method for the two-dimensional extended Boussinesq equations. *International Journal for Numerical Methods in Fluids* 2002; **39**:865–885.
12. Li YS, Liu S-X, Yu Y-X, Lai G-Z. Numerical modeling of Boussinesq equations by finite element method. *Coastal Engineering* 1999; **37**:97–122.
13. Woo S, Liu PL-F. A Petrov–Galerkin finite element model for one-dimensional fully nonlinear and weakly dispersive wave propagation. *International Journal for Numerical Methods in Fluids* 2001; **37**:541–575.
14. Wei G, Kirby JT. Time-dependent numerical code for extended Boussinesq equations. *Journal of Waterway, Port, Coastal, and Ocean Engineering* 1995; **121**:251–261.
15. Zhao DH, Shen HW, Tabios III GQ, Lai JS, Tan WY. Finite-volume two-dimensional unsteady-flow model for river basins. *Journal of Hydraulic Engineering* 1994; **120**:863–882.
16. Zhao DH, Shen HW, Lai JS, Tabios III GQ. Approximate Riemann solvers in FVM for 2D hydraulic shock wave problems. *Journal of Hydraulic Engineering* 1996; **122**:692–702.
17. Mingham CG, Causon DM. High-resolution finite-volume method for shallow water flows. *Journal of Hydraulic Engineering* 1998; **124**:605–614.
18. Mingham CG, Causon DM. Calculation of unsteady bore diffraction using a high resolution finite-volume method. *Journal of Hydraulic Research* 2000; **38**:49–56.
19. Frazão SS, Zech Y. Undular bores and secondary waves-experiments and hybrid finite-volume modelling. *Journal of Hydraulic Research* 2002; **40**:33–43.
20. Roe PL. Approximate Riemann solvers, parameter vectors, and difference schemes. *Journal of Computational Physics* 1981; **43**:357–372.
21. Yamamoto S, Kano S, Daiguji H. An efficient CFD approach for simulating unsteady hypersonic shock–shock interference flows. *Computers and Fluids* 1998; **27**:571–580.
22. Bermúdez A, Dervieux A, Desideri J-A, Vázquez ME. Upwind schemes for the two-dimensional shallow water equations with variable depth using unstructured meshes. *Computer Methods in Applied Mechanics and Engineering* **155**:49–72.
23. Vázquez-Cendon ME. Improved treatment of source terms in upwind schemes for the shallow water equations in channels with irregular geometry. *Journal of Computational Physics* 1999; **148**:497–526.
24. Brufau P, Vázquez-Cendon ME, García-Navarro P. A numerical model for the flooding and drying of irregular domains. *International Journal for Numerical Methods in Fluids* 2002; **39**:247–275.
25. Zhou JG, Causon DM, Mingham CG, Ingram DM. The surface gradient method for the treatment of source terms in the shallow-water equations. *International Journal for Numerical Methods in Fluids* 2001; **168**:1–25.
26. Abbott MB, Minns AW. *Computational Hydraulics* (2nd edn). Ashgate: U.S.A., 1998.
27. Erduran KS, Kutija V, Hewett CJM. Performance of finite-volume solutions to the shallow water equations with shock-capturing schemes. *International Journal for Numerical Methods in Fluids* 2002; **40**:1237–1273.
28. Toro EF. *Riemann Solvers and Numerical Methods for Fluid Dynamics*. Springer: Berlin, 1997.
29. Alcrudo F, García-Navarro P, Saviron J-M. Flux difference splitting for 1D open channel flow equations. *International Journal for Numerical Methods in Fluids* 1992; **14**:1009–1018.
30. Mingham CG, Causon DM. On high resolution finite-volume modelling of discontinuous solutions of the shallow water equations. *Proceedings of the 1997 3rd International Conference on Modelling of Seas and Coastal Regions*, La Coruna, Spain, 1997; 43–52.
31. Hirch C. *Numerical Computation of Internal and External Flows*, vol. 2. Wiley: U.K., 1990.
32. Hu K, Mingham CG, Causon DM. Numerical simulation of wave overtopping of coastal structures using the non-linear shallow water equations. *Coastal Engineering* 2000; **41**:433–465.
33. Li YS, Liu S-X, Wai OWH, Yu Y-X. Wave concentration by a navigation channel. *Applied Ocean Research* 2000; **22**:199–213.
34. Bradford SF, Sanders BF. Finite-volume models for unidirectional, nonlinear dispersive waves. *Journal of Waterway, Port, Coastal, and Ocean Engineering* 2002; **128**:173–182.

